Journal of Electric Propulsion

RESEARCH Open Access

# A radio-frequency generator for ion thrusters based on a Class-E power circuit

Edwin Beller*, Christian Roessler, Uwe Probst, Rainer Thueringer and Chris Volkmar

*Correspondence:
edwin.beller@nanop.thm.de
Center of Competence for Nanotechnology and Photonics (NanoP), TH Mittelhessen University of Applied Sciences, Wiesenstrasse 14, Giessen, 35390, Hessen, Germany

**Abstract**

Operating a radio-frequency ion thruster (RIT) requires a high frequency current flowing through an induction coil in order to ignite and maintain an inductively coupled plasma discharge (ICP). Several methods to create that current have been demonstrated and evaluated regarding complexity, flexibility and efficiency. Especially in space applications reliability and minimal power loss is crucial to comply to strict mission requirements. As one of the leanest concepts in terms of required components and nevertheless highest possible efficiency, the Class-E power circuit has proven itself as a well suited radio-frequency generator (RFG) of a RIT system. However, electrical performance and especially electromagnetic compatibility (EMC) during operation have not been evaluated, but are essential if the system is intended for use in space. In order to fill this gap and bring the Class-E circuit into the fold of established RFG concepts, a prototype was designed, built, and used to operate a RIT-10. For reference, a conventional Half-Bridge RFG was tested under the same operating conditions. Further investigations are concerned with EMC behaviour of both devices and show that Class-E circuit exhibits significantly lower electromagnetic emission during operation compared to the Half-Bridge reference.

**Keywords:** Class-E power amplifier, Radio-frequency ion thruster, Inductively coupled plasma, Electromagnetic compatibility

## Introduction

Since the invention of radio-frequency ion thrusters (RIT) in the 1960s [1] this technology has become a promising part in electric spacecraft propulsion. Several operational satellite projects proved its suitability in terms of North-South-Station Keeping and even orbit raising [2]. Compared to other concepts of gridded ion-thruster propulsion systems [3] the RIT ignites an inductively coupled plasma inside a discharge vessel [4], which is illustrated in Fig. 1.

To maintain that discharge, energy is transferred through a sinusoidal current $\widetilde{I}$ with a frequency depending on thruster size in the range between 0.5 MHz and 2 MHz to the induction coil. Usually, this current is formed from a DC voltage by a radio frequency generator (RFG) [5]. According to Faraday's law, the changing magnetic field $\frac{-\mathrm{d}\vec{B}}{\mathrm{d}t}$ created

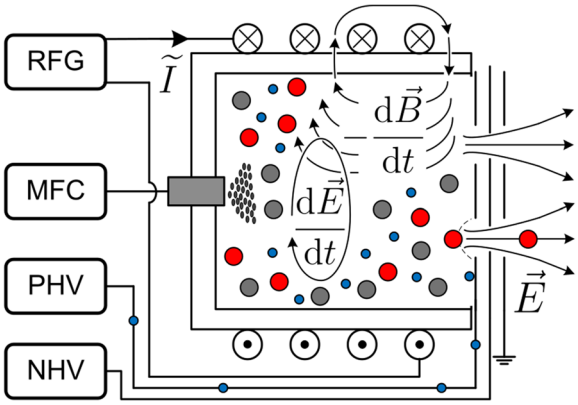


**Fig. 1** Operating principle of a RIT with neutral particles (gray), positive charged ions (red) and electrons (blue) forming a plasma inside a discharge vessel. Energy is transferred by an RF current $\widetilde{I}$ generating a changing magnetic Field $\frac{-d\vec{B}}{dt}$, which in turn induces an changing electric field $\frac{d\vec{E}}{dt}$ accelerating electrons for impact ionization. A static electric field $\vec{E}$ extracts the positive charged ions from the plasma. The peripheral components are abbreviated as follows: Radio-Frequency Generator (RFG), Mass Flow Controller (MFC), Positive High Voltage (PHV), Negative High Voltage (NHV)

by the coil current $\widetilde{I}$ induces a perpendicular electric Field $\frac{d\vec{E}}{dt}$ which is capable of accelerating electrons and turn neutral gas particles into positive charged ions due to impact **ionization**. An electrostatic field $\vec{E}$ formed by a grid system accelerates the ions out of the thruster (**extraction**). In order to fulfill charge conservation inside the plasma, electrons are attracted by the positive potential of the first grid adjacent to the plasma (called screen grid) which results in a positive current provided by the positive high voltage supply (PHV).

## State of the art concepts

Various concepts can be considered when designing a RFG, some of which are presented in [5–7]. Table 1 provides an overview of existing concepts and also includes the proposed approach.

### Half-Bridge circuit

A popular concept realizing a RFG is the analog controlled Half-Bridge topology (HBA) [9]. In conjunction with a RIT there are several flight proven designs in which the HBA topology is implemented as a part of the thruster assembly [2]. Figure 2a shows the electrical equivalent circuit of the Half-Bridge circuit. In order to classify complexity and, based on this, the reliability, not only the number of electrical components but also their positions inside the circuit must be taken into account. Referring to Fig. 2a, the Half-Bridge circuit consists of two semiconductor switches, here denoted as S1 and S2. Due

**Table 1** RFG topology overview

| Concept | Control strategy | Complexity[a] | Operating range | References |
|---|---|---|---|---|
| Half-Bridge (HBA) | analog (PLL) | medium | variable/fixed | [8–10] |
| Half-Bridge (HBD) | digital (FPGA) | high | variable | [5, 7] |
| Royer-Converter (RCA) | analog | medium | variable | [11] |
| Royer-Converter (RCD) | digital (FPGA) | high | variable | |
| Class-E | analog | low | fixed | [12–14] |

[a] Qualitative classification considering component count, control algorithm and switch configuration

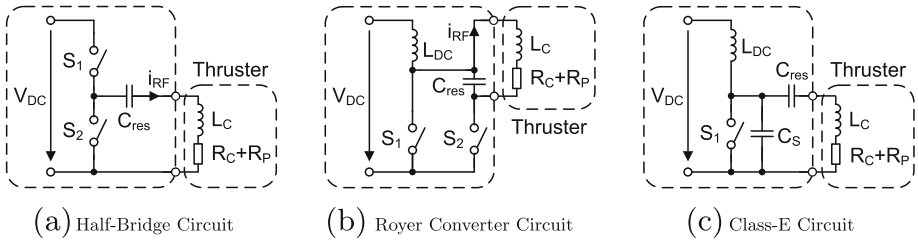


**Fig. 2** RFG Power Circuit Concepts

to a floating source potential of switch S1 during operation, additional active peripheral components are required to ensure functionality of the Half-Bridge which increases complexity of the circuit. Beside switches only one additional capacitor $C_{\mathrm{res}}$ is necessary to form a series resonant circuit in conjunction with the inductive load and complete the Half-Bridge based RFG.

#### Royer converter circuit

An alternative design called Royer-Converter is the scope of another work [11] and shown in Fig. 2b. It evades the utilization of a switch with floating source potential and thereby decreases the number of peripheral components compared to the Half-Bridge circuit. Nevertheless, two active switches and an additional choke $L_{\mathrm{DC}}$ are required for operation. The resonant circuit is formed by a capacitance $C_{\mathrm{res}}$ resulting in a parallel resonance. Half-Bridge and Royer-Converter both offer the opportunity of being operated in a closed control loop [5, 7–9] to counteract load deviations which result from changing plasma parameters and maintain operation with minimal power loss. Analog and digital concepts can be considered to continuously adapt the switching frequency in order to ensure optimal converter operation with minimum losses under various load conditions and operating points. Sophisticated solutions based on digital FPGAs were developed enabling the definition of switching events with a maximum time resolution in the single digit nanosecond range [5, 7]. Thereby soft switching techniques with the highest accuracy can be implemented. Furthermore, the output power of the converter can be adjusted digitally using certain modulation schemes [7, 15]. However, both converter types can also be operated at fixed frequency which reduces the amount of components required, but limits the operating range and ties the design to a single load case. On the other hand, the complexity of the system is drastically reduced without the need for a digital closed-loop control matching switching frequency of the power circuit and resonance frequency of the load. Especially in space applications this can save the cost of elaborate qualification tests and expensive radiation hardened and high-reliability components, particularly in conjunction with FPGAs.

### Class-E power Circuit

The Class-E circuit has become popular in radar and radio transmission applications [16] due to its high efficiency and simple circuit structure. As shown in Fig. 2c, the circuit consists of an additional shunt capacitor $C_{\mathrm{S}}$ when compared to the royer converter but uses only one active switch. This renders the Class-E circuit advantageous as no synchronisation of the switches is required and as active components are more susceptible to ionizing radiation. There have been numerous examples on control methods for Class-E circuit

[17–19] but due to reasons mentioned in the previous chapter a low complexity design is chosen.

### Theory of operation

Similar to the other topologies, the Class-E circuit is capable of soft switching which is achieved if the voltage across the capacitor $C_S$ is zero during switching. This is also referred to as zero voltage switching (ZVS) and avoids switching loss as no stored energy in the capacitor is dissipated in the on-resistance $r_{DS}$ as heat. Furthermore, it mitigates electromagnetic radiation because fast transient currents are prevented which are a common source of electromagnetic interference. The Class-E circuit will fulfil ZVS and zero voltage derivative switching (ZVDS) for a specific load impedance $Z_{nom}$, if design equations Eqs. 1 to 3 are correctly applied so that $Z_{nom}$ equals $Z_{Load}$ where ideally $R_{Load} = R_{c+pl}$, $X_{Load} = \omega L_{c+pl} - 1/(\omega C_{res})$ and the ripple is $\gamma = \Delta i_L / I_{DC} < 10\,\%$ [20].

$$R_{nom} = \frac{8}{\pi\left(\pi^2+4\right)}\frac{1}{\omega C_S} \tag{1}$$

$$X_{nom} = \frac{\pi^2-4}{2\left(\pi^2+4\right)}\frac{1}{\omega C_S} \tag{2}$$

$$L_{DC} = \frac{1}{\omega\gamma}\frac{1}{\omega C_S} \tag{3}$$

ZVDS prevents a commutation from capacitor current $i_c$ to drain-source current $i_{DS}$ thus avoiding further fast transient currents. This facilitates presumably good electromagnetic compatibility (EMC) by design. Hence, this desirable type of operation will be referred to as nominal operation and its waveforms are shown in Fig. 3. With varying load impedance $Z_{Load}$, the Class-E circuit will operate outside nominal conditions with four different and distinctive drain-source voltage $v_{DS}$ waveforms, which are separated by the impedance of either condition in Eqs. 4 and 5 [21] as shown in Fig. 4 :

$$(\omega C_S R_{ZVS})^2 + \left(\omega C_S X_{ZVS} - \frac{\pi^2-4}{2\pi^2}\right)^2 = \frac{4}{\pi^4} \tag{4}$$

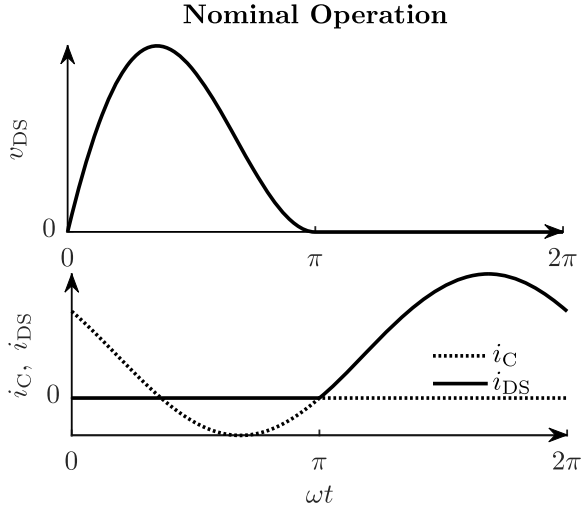


**Fig. 3** Waveforms during nominal operation of the Class-E circuit with a duty cycle of 50 %

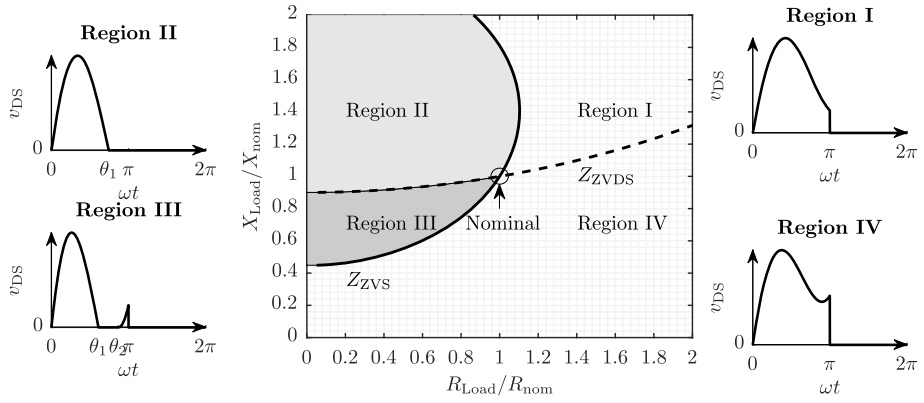


**Fig. 4** Switching-pattern distribution for the Class-E circuit on a complex $Z_{\mathrm{Load}}/Z_{\mathrm{nom}}$ plane with characteristic example waveforms for a duty cycle of 50 %

$$(\omega C_{\mathrm{S}} R_{\mathrm{ZVDS}})^2 + (\omega C_{\mathrm{S}} X_{\mathrm{ZVDS}} - 1)^2 = \frac{1}{4} + \frac{4}{\pi^2} \tag{5}$$

Visually, the waveforms are distinguishable by whether the voltage reached zero volts and by the slope during turn-on switching. If all load impedances are contained within region II, the Class-E circuit will operate with ZVS due to the MOSFET body diode yielding the aforementioned benefits.

### Design guidelines

Every load impedance associated with a plasma operating point can be shifted by adjusting the serial capacitance $C_{\mathrm{res}}$ to compensate the reactive load $X_{\mathrm{Load}}$ and by adjusting the shunt capacitance $C_{\mathrm{S}}$ to scale the nominal impedance $Z_{\mathrm{nom}}$. Therefore it is possible to shift every operating point to region II. Although presumably beneficial for EMC, a more efficient operation of the RFG may exist in other regions. By simulations or run-time efficient analytic models [22], an optimization can be performed utilizing a hill climbing algorithm to determine the most efficient value for both capacitors. Nevertheless, both approaches require an accurate knowledge about the load parameters as well as parasitic resistances. These load parameters can be determined by measuring RITs at varying operating points using existing RFGs. A thorough explanation of this will be given in Performance mapping. Still, parasitic resistances of the RFG can only be assumed with the parameters given in the data sheet before construction. Therein lies the difficulty of optimizing Class-E RFGs with multiple operation points a priori.

In the following analysis a Class-E RFG was designed to incorporate a near nominal operation for a mass efficient setting of a RIT-10. Beforehand, its necessary load impedances $Z_{\mathrm{Load}}$ were measured in accordance with the procedure described in Performance mapping. The results plotted in the switching-pattern distribution are shown in Fig. 5. Furthermore, to ensure better comparability with the Half-Bridge RFG, the same GaN transistor of type GS61008T was implemented in our Class-E RFG.

## Experimental setup

### Performance mapping

In order to verify its function and operation range, the Class-E RFG operates a RIT-10 inside a vacuum chamber as described in [4]. Mass Flow Controller, Positive High Voltage,

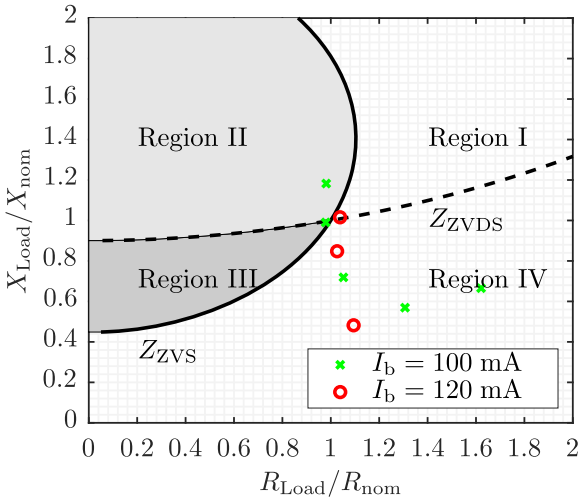


**Fig. 5** Load impedances of a RIT-10 applied to the switching-pattern distribution of our Class-E RFG with varying mass flow and beam current $I_{\mathrm{b}}$. For high mass efficiency $Z_{\mathrm{nom}} \simeq Z_{\mathrm{Load}}$ holds true

Negative High Voltage and RFG are located outside the chamber and supply the thruster via vacuum feedthroughs. A triaxial cable with a length of approximately 1 m is used to transfer RF energy from RFG to the induction coil. The xenon mass flow is varied in the range of 1.55 sccm to a maximum of 4 sccm depending on the beam current.

Typically, a performance mapping classifies the generated thrust in terms of propellant utilization or mass flow and the required RF power, shown in Fig. 8. Since thrust measurements are costly, beam current is a common measure that is kept constant at a given mass flow by adjusting the RF power provided to the induction coil. The beam current can be easily determined by measuring the DC current to the extraction grids generated by PHV and NHV supplies.

With regard to RFG load impedance, the plasma resistance $R_{\mathrm{pl}}$ strongly depends on the mass flow, that determines the mean free path length of the neutral propellant particles and mobile electrons inside the discharge chamber. Furthermore, $R_{\mathrm{pl}}$ is affected by the cross-section describing the electron-neutral-interaction, that shows a nonlinear dependence on the kinetic energy of the electrons. All these effects lead to different load impedance at different operating points during a performance mapping.

To compare performance, efficiency and EMC of the proposed Class-E RFG, all measurements are conducted with a Half-Bridge (HBD) RFG in the same manner. Since the provided input power $P_{\mathrm{RFG}}$ is measured and used in the performance mapping, the electrical efficiency of the different RFG concepts can be assessed immediately, with a smaller input power representing a higher efficiency for the same beam current.

Performance mappings of both RFGs establish comparability between electrical measurements and show the required DC input power of the RFG to generate a certain beam current and thus thrust. An alternative benchmark is the electrical efficiency of both RFGs determined by VI-Probes [23]. However this type of active power measurement can be inaccurate due to high phase angles between RF current and voltage. Particularly with high quality factor of the induction coil, the phase angle approaches 90 degrees which in conjunction with the devices accuracy of $\pm 1$ deg leads to erroneous phase measurements.

Hence, the performance mapping was used as benchmark with the setup illustrated in Fig. 6.

Nevertheless VI-Probes by Impedans were used to obtain rough estimates of both the plasma as well as RF Cable 2 impedance at selected RIT-10 operating points. The first measurements were performed with the HBD RFG and utilized to calculate $X_{\mathrm{Load}}$ and $R_{\mathrm{Load}}$ for a first Class-E design determining $C_{\mathrm{S}}$ and $C_{\mathrm{Res}}$. However, in operation the $\nu_{\mathrm{DS}}$ waveforms of the oscilloscopes were marginally different from the waveform, which were simulated with the measured load impedances. It was assumed that RF Cable 1 and RF VI-Probe are accountable for this and that they can be approximated by an inductive series impedance. After this impedance had been determined, the comparable load impedances $Z_{\mathrm{Load}}$ could be recorded, which are no longer dependent on the cabling and can be used for optimizing the design. The exact identification of $Z_{\mathrm{Load}}$ is important, because the latter will differ due to a different cabling, which inevitably occurs during the subsequent setup in the context of the EMC test.

The performance mapping and load impedance measurements pursue as follows. A defined mass flow is set by the MFC and the Beam Current Controller adjusts the RFG DC input power until the target value is reached. Operating points are considered stable if the fluctuation of RFG DC input power within a period of 10 minutes is smaller than 0.5 % which is also the condition to record measurement data. Additionally, the RF current, voltage and phase angle measurements are recorded to determine the load impedance $Z_{\mathrm{Load}}$ for the current test case.

#### Electromagnetic compatibility

Further investigations on electromagnetic interference have been carried out. Both RFG concepts were evaluated for their electromagnetic emission using a Gigahertz Transverse Electromagnetic (GTEM) cell [24] at three different operating points. It enables extrapolation of far field electromagnetic fields generated by electrical devices in small confined spaces. Emission identification was performed in the frequency range of 30 MHz to 1 GHz with a 6 dB bandwidth of 120 kHz and 1 ms dwell time.

Since we had no access to a vacuum chamber adjacent to the GTEM cell, the plasma impedance measured during the previously conducted performance mapping was replicated by utilizing a load emulator. This device consists of a coil with an adjustable coil tap and immersible iron core. It enables an adjustment of $L_{\mathrm{Load}}$ and $R_{\mathrm{Load}}$ to the specified values obtained during the performance mapping. Additionally the length of RF Cable 1 had to be elongated to insert the RFG into the GTEM cell. After the impedance of RF Cable 1 and the VI-probe was determined, the latter was used to set the load impedance more easily. This entire setup is illustrated in Fig. 7.

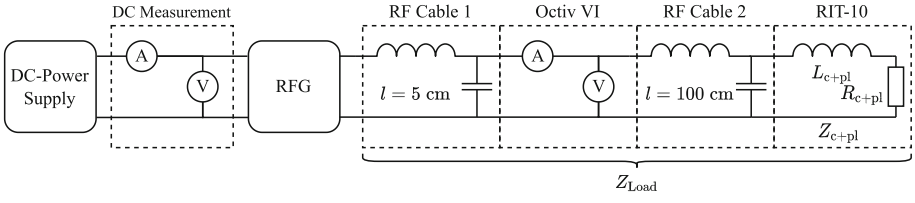


**Fig. 6** Schematic of the electrical setup used during performance mapping and load impedance identification

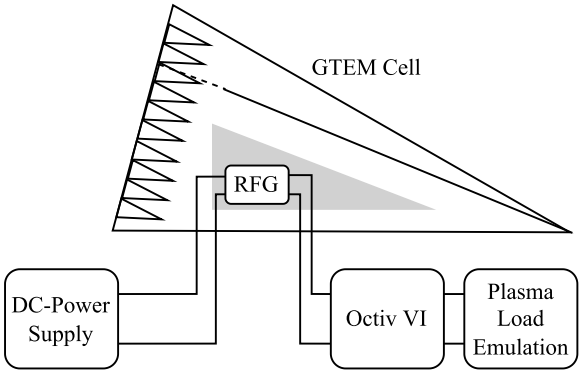


**Fig. 7** Schematic of the electrical setup for EMC testing with adjusted cable lengths

## Results

### Performance mapping

Two performance mappings were taken respectively for the HBD RFG and Class-E circuit each at different beam currents, shown in Fig. 8. The power consumption at each beam current is either similar or slightly higher for the Class-E RFG when compared to the HBD RFG. Specifically the operating points at 2 sccm, 120 mA and 1.5 sccm, 100 mA are marginally more efficient when utilizing the Class-E RFG. The selection of mass flow data points for this performance mapping is chosen to have similar mass efficiencies at both beam currents, as shown in Table 2. The resulting load impedance and switching-pattern region are displayed as well. According to TC 6, $L_{\mathrm{Load}}$ and $R_{\mathrm{Load}}$ corresponding to a beam current of 120 mA at 1.9 sccm xenon mass flow were used as the operating point for nominal Class-E circuit design.

The Class-E waveforms for some selected operating points are presented in Fig. 9. Near nominal operation is reached for a mass flow of 1.9 sccm and beam current of 120 mA or 1.65 sccm and 100 mA respectively. All operating points follow their characteristic waveforms as described in Fig. 5. Most notably, there is ringing during turn-off which can be attributed to the rapidly changing drain-source current $i_{\mathrm{DS}}$ resulting in voltage oscillations due to the parasitic inductances of the transistor and PCB design. This exemplifies

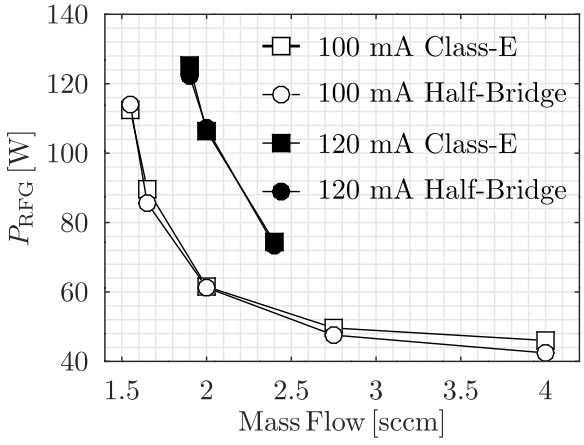


**Fig. 8** Performance mapping of the two different RFG concepts powering a RIT-10. The setup is operated at two different beam currents for HB RFG and Class-E RFG each. Grid voltages were set as follows: $V_{\mathrm{Screen}} = 1200\,\mathrm{V}$, $V_{\mathrm{ACC}} = -150\,\mathrm{V}$

**Table 2** Selection of operating points and corresponding mass efficiency

| TC[a] | $I_{beam}$ [mA] | $\dot{m}$ [sccm] | ME[b] [%] | $L_{Load}$ [$\mu$H] | $R_{Load}$ [$\Omega$] | Class-E Region |
|---|---|---|---|---|---|---|
| 1 | 100 | 2.00 | 70 | 5.413 | 1.211 | IV |
| 2 | 120 | 2.40 | 70 | 5.371 | 1.273 | IV |
| 3 | 100 | 1.65 | 84 | 5.477 | 1.103 | II |
| 4 | 120 | 2.00 | 84 | 5.444 | 1.159 | IV |
| 5 | 100 | 1.55 | 90 | 5.506 | 1.059 | II |
| 6 | 120 | 1.90 | 88 | 5.470 | 1.127 | Nom. |

[a] Test Case
[b] Mass Efficiency

that the turn-off remains a source of potential electromagnetic emissions for the Class-E circuit despite being optimized for ZVS/ZVDS during turn-on. However in this particular case, the coaxial cable used to measure $v_{DS}$ waveforms was the reason for the ringing.

### Electromagnetic compatibility

Figure 10 compares the interference spectra of Class-E circuit and HB at nominal operation corresponding to Table 2 TC 6. The electrical field strength $E$ is significantly smaller for almost every measured frequency. Especially in the range between 30 MHz and 90 MHz the Class-E circuit shows negligible field strengths whereas the HB topology reveals strong peak values at the higher order harmonics of the switching frequency. This can be attributed to the rectangular shaped voltage waveform including high voltage slopes generated at the Half-Bridge output and forwarded to the RF cable supporting electromagnetic emission. In contrast, the Class-E circuit shows a smaller voltage slope and an entirely smoother waveform when operated at nominal design parameters, illustrated in Fig. 9. However, a sharp edge in the voltage waveform can also be generated with the Class-E circuit besides nominal operation when the drain-source voltage is tied hard to zero, i.e. during region IV operation presented in Fig. 9. A comparison of the individual Class-E circuit operating modes regarding electromagnetic emission is given in Fig. 11. For a better representation of the different operating regions, the spectra of region II and IV are shifted by an offset. This allows a more detailed examination of individual areas in which the radiation characteristics differ.

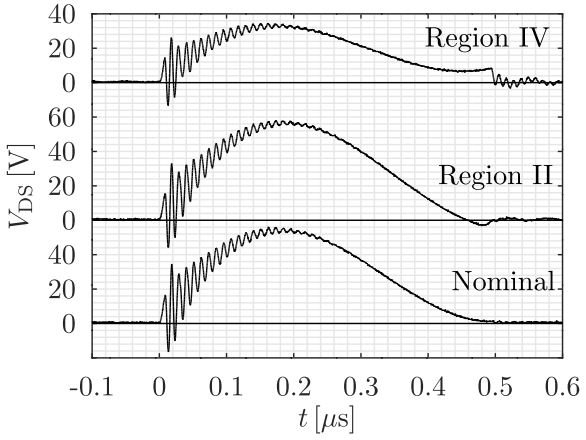


**Fig. 9** Drain-source voltage of Class-E circuit during blocking phase operating at different loads. Region IV operation and TC 4, Region II operation and TC 5, nominal operation and TC 6 are described in Table 2

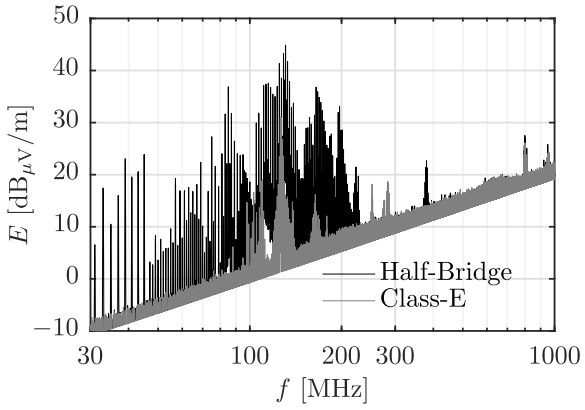


**Fig. 10** Comparison of Class-E and Half-Bridge emission spectra operating at TC 6 as described in Table 2. Noticeably high field strengths around 800 MHz and 950 MHz measured in both spectra are caused by German mobile network due to non-ideal shielding of the GTEM cell

With regard to nominal operation, additional spectral lines appear below 200 MHz operating in region II and even below 100 MHz during region IV operation. Table 3 provides an overview of all the setups carried out as part of the EMC measurements.

In order to easily compare and evaluate the recorded EMC results, the spectra are merged into one measure $E_{\text{mean}}$ by integrating field strengths over frequency, dividing by measured bandwidth and subtracting the mean electric field strength of the empty measurement to account exclusively for the emission radiated by the device under test. The procedure is stated in Eq. 6 with $\Delta f$ describing the observed frequency range:

$$E_{\text{mean}} = \frac{1}{\Delta f} \int_{\Delta f} (E - E_{\text{Empty}})\, \mathrm{d}f \tag{6}$$

Since the generated electric field strength scales with the power provided to the device under test, an additional figure of merit (FOM) is introduced that relates the mean electric field to the input power fed to the RFG:

$$FOM = \frac{E_{\text{mean}}}{P_{\text{RFG}}} \tag{7}$$

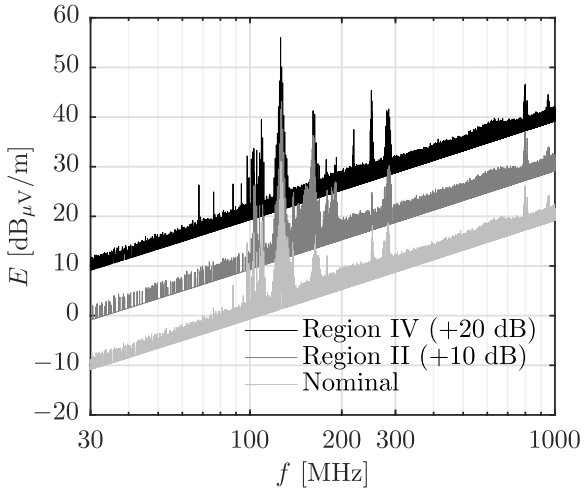


**Fig. 11** Radiated electric field of Class-E operating at different loads during region IV operation at TC 4, region II operation at TC 5 and nominal operation at TC 6 according to Table 2

**Table 3** Mean electric field strength $E_{mean}$ for conducted test cases inside GTEM cell

| Setup | TC[a] | $P_{RFG}$ [W] | $E^{b}_{mean}$ [$\mu$V/m] | $FOM^{c}$ $\left[\frac{10^{-9}}{Am}\right]$ |
|---|---|---|---|---|
| Empty | NA | 0 | 0 | NA |
| Class-E, AUX-Supply | NA | 0 | 0.106 | NA |
| Half-Bridge, AUX-Supply | NA | 0 | 0.379 | NA |
| Class-E,nominal | 6 | 126 | 0.302 | 2.39 |
| Half-Bridge, nominal | 6 | 125 | 1.275 | 10.20 |
| Class-E, Region IV | 4 | 60 | 0.424 | 7.07 |
| Half-Bridge, Region IV | 4 | 59 | 13.800 | 233.83 |
| Class-E, Region II | 5 | 112 | 0.206 | 1.84 |
| Half-Bridge, Region II | 5 | 113 | 2.310 | 20.44 |

[a] Test Case according to Table 2
[b] Mean electric field strength of measured spectrum
[c] Mean electric field strength in relation to input power $P_{RFG}$ used as figure of merit

Classifying EMC behavior of Class-E and HBD RFG, emission characteristics are significantly higher during HBD operation. This is due to comparatively sharp edges with high voltage slope which occurs in a Half-Bridge circuit during a switching event, resulting in higher order harmonics with larger magnitude. In contrast, the Class-E circuit shows smooth waveforms avoiding higher order harmonics when operated near nominal design parameters. However, during region IV operation the emission evaluated by FOM is more than three times larger compared to nominal or region II operation. With respect to Fig. 9, when the switch is turned on in region IV, $v_{DS}$ is hard switched to zero. In consequence, higher order harmonics are generated which favor radiation supported by cables outside or copper tracks inside the RFG. Nonetheless, the Class-E turns out to generate less radiated emissions even at this point of operation compared to the HBD.

## Conclusion

In this paper, a Class-E circuit has been successfully developed to operate a RIT-10 in typical points of operation. Compared to a Half-Bridge RFG it shows similar performance regarding electrical efficiency but requires only one active switch inside the power circuit. This results in a significant reduction of the number of components, decreasing complexity and, in consequence, raising reliability. Especially in space applications this enables cost savings in the expensive field of radiation hardened components, eases qualification processes and thus enables a significant reduction in costs. On the other hand a detailed knowledge of the load parameters determined by thruster setup, coil structure and cable connection is essential for design when utilizing a Class-E circuit with RIT. Nominal operation can only be ensured for a single load impedance, which is influenced by thruster geometry, cable length, propellant and mass flow. Furthermore, the Class-E circuit shows significant advantages regarding electromagnetic emission due to its switching behaviour. Even in sub optimum operation, the Class-E circuit can sustain advantageous EMC characteristics in certain limits. Overall, it proves to be a cost-saving and radiation-compatible RFG topology and thus a serious alternative to conventional RFG concepts, provided that the design is adapted to the entire thruster environment including numerous dependencies that must be taken into account for proper operation as shown in this paper.

**Acknowledgement**
This publication represents a component of the corresponding author's doctoral thesis in the Department of Physics at the Justus-Liebig-University Giessen, Germany in cooperation with Technische Hochschule Mittelhessen - University of Applied Sciences at the Graduate Centre of Engineering Sciences at the Research Campus of Central Hessen.

**Authors' contributions**
E.B. and C.R. performed the measurements, evaluated the results, wrote the main text of the manuscript, and prepared the figures. R.T. contributed to the EMC measurements and gave practical advice in performing and evaluating the results. C.V. supervised the project and all measurements, gave practical advice during the measurements, the evaluation of the results, and the preparation of the manuscript. U.P. gave practical advice during the evaluation of the results and the preparation of the manuscript. All authors read, reviewed, and commented on earlier versions of the manuscript and approved the final manuscript.

**Funding**
This project was financed by the funding program "Forschung für die Praxis" of the Hessian Ministry for Science and Art. Open Access funding enabled and organized by Projekt DEAL.

**Availability of data and materials**
Supplemental data, not stated within this article, that support the findings of this study are available from the corresponding author, E.B., upon reasonable request.

## Declarations

**Ethics approval and consent to participate**
Not applicable.

**Consent for publication**
Not applicable.

**Competing interests**
The authors declare that they have no competing interests.

Received: 25 April 2022 Accepted: 5 July 2022
Published online: 01 September 2022

**References**

1. Loeb HW (1962) Ein Elektrostatisches Raketentriebwerk mit Hochfrequenzionenquelle; Astronautica Acta Vol. VIII, Fasc 1. p 49
2. Killinger R, et al (2000) RITA Ion Propulsion for Artemis Lifetime Test Results. https://doi.org/10.2514/6.2000-3273
3. Sneyder, et al (2010) Performance Evaluation of the T6 Ion Engine. AIAA Joint Propulsion Conference Exhibit. https://doi.org/10.2514/1.B34173
4. Leiter H, et al. (2002) Evaluation Of The Performance Of The Advanced 200 mN Radiofrequency Ion Thruster RIT XT. J Spacecr Rockets. https://doi.org/10.2514/6.2002-3836
5. Simon J (2016) Entwicklung und Aufbau eines Radiofrequenzgenerators zur Versorgung und elektrischen Charakterisierung induktiv-gekoppelter Plasmen in Radiofrequenz-Ionentriebwerken. Justus-Liebig-Universität, Giessen. http://geb.uni-giessen.de/geb/volltexte/2017/12283
6. Holste K, et al. (2020) Ion thrusters for electric propulsion: Scientific issues developing a nichetechnology into a game changer. Rev Sci Instrum. https://doi.org/10.1063/5.0010134
7. Simon J, et al. (2016) Development of a Radio-Frequency Generator for RF Ion Thrusters. Trans Jpn Soc Aeronaut Space Sci Aerosp Technol Jpn 14. https://doi.org/10.2322/tastj.14.Pb_33
8. Failing O (1985) HF-Generator mit Leistungs-MOSFETs (German) [HF generator with power mosfets]. Elektronik 15/26.7.1985:61–65
9. Kadrnoschka W, et al. (2008) High frequency generator for ion and electron sources. Europ. Patent No. EP 2 020 672 B1:9–11
10. Holste K, et al. (2018) Performance of an iodine-fueled radio-frequency ion-thruster. Eur Phys J D. https://doi.org/10.1140/epjd/e2017-80498-5
11. Reeh A (2019) Control Circuit For An Oscillator Circuit For Operating Parallel-Fed Oscillators. Europ. Patent No. EP 3 667 917 A1:1–10
12. Ewing G (1965) High-Efficiency Radio-Frequency Power Amplifiers. PhD thesis, Oregon State University
13. Raab F (1977) Idealized Operation of the Class E Tuned Power Amplifier. IEEE Trans Circ Syst. https://doi.org/10.1109/TCS.1977.1084296
14. Dudin S, Rafalsky D (2020) Radio-Frequency Generator For Plasma Source And Method For Adjusting The Same. Europ. Patent No. EP 3 754 187 A1
15. Surminskii A, et al. (2019) Development of a compact high efficiency RF generator forinductive coupled plasma sources
16. Mediano A, Ortega-González F (2018) Class-E Amplifiers and Applications at MF, HF and VHF. IEEE Microw Mag. https://doi.org/10.1109/MMM.2018.2823238
17. Reatti A, Corti F, Pugi L, Kazimierczuk M, Migliazza G, Lorenzani E (2018) Control Strategies for Class-E Resonant Inverter with Wide Load Variation. In: 2018 IEEE International Conference on Environment and Electrical Engineering

and 2018 IEEE Industrial and Commercial Power Systems Europe (EEEIC / I CPS Europe). pp 1–6. https://doi.org/10.1109/EEEIC.2018.8494505
18. Moffatt R, Howarth T, Gafner C, Yen J, Chen F-K, Yu J (2019) A Distributed, Phase-locked, Class-E, RF Generator with Automatic Zero-Voltage Switching. In: 2019 IEEE Wireless Power Transfer Conference (WPTC). pp 390–394. https://doi.org/10.1109/WPTC45513.2019.9055602
19. Komiyama Y, Matsuhashi S, Zhu W, Mishima T, Ito Y, Uematsu T, Nguyen K, Sekiya H (2021) Frequency-Modulation Controlled Load-Independent Class-E Inverter. IEEE Access 9:144600–144613. https://doi.org/10.1109/ACCESS.2021.3121781
20. Kazimierczuk M (2015) RF Power Amplifiers, Second Edition. https://doi.org/10.1002/9781118844373
21. Ohira T (2020) Load impedance perturbation formulas for class-E power amplifiers. IEICE Commun Express. https://doi.org/10.1587/comex.2020XBL0085
22. Nagashima, et al. (2014) Waveform equations, output power, and power conversion efficiency for class-e inverter outside nominal operation. IEEE Trans Ind Electron. https://doi.org/10.1109/TIE.2013.2267693
23. Scullin P, Hopkins M (2014) U.S. Patent Application for ŞAnalysing RF Signals from a Plasma System,Ť Docket No. WO2014016357 A3, filed 24 July 2013
24. Budania M, Verma G, Jeyakumar A (2020) Design and analysis of GTEM cell using CST studiosimulation. IEEE Int Conf Electron Comput Commun Technol (CONECCT). https://doi.org/10.1109/CONECCT50063.2020.9198456

## Publisher's Note